Pergamon

Int. J. Solids Structures Vol. 33, No. 2, pp. 221–248, 1996
Copyright © 1995 Elsevier Science Ltd
Printed in Great Britain. All rights reserved
0020–7683/96 $9.50 + .00

0020–7683(95)00033–X

ANALYSIS OF BERKOVICH INDENTATION

P.-L. LARSSON† and A. E. GIANNAKOPOULOS
Department of Solid Mechanics, Royal Institute of Technology, S-10044 Stockholm, Sweden

E. SÖDERLUND and D. J. ROWCLIFFE
Department of Materials Science and Engineering, Royal Institute of Technology, S-10044 Stockholm, Sweden

R. VESTERGAARD
Department of Solid Mechanics, Technical University of Denmark, Lyngby, Denmark

(*Received* 26 *August* 1994; *in revised form* 8 *February* 1995)

Abstract—The Berkovich indentation test is analysed numerically, using the finite element method, and experimentally. The results derived are pertinent to indentation of elastic materials and metals and include universal formulae for the load-indentation depth relation and the hardness, as well as a detailed study of the mechanical fields involved at loading and unloading. Large strain elastic and elastoplastic results are compared with small strain ones and similarities, as well as differences, are discussed in some detail. Special attention is given to a comparison between the characteristics of Berkovich indentation and the Vickers hardness test. The accuracy of relevant formulae for determining the elastic stiffness during the unloading process is checked. Experiments are performed both on the nano- and microscale. Numerical and experimental findings are compared in detail, especially as regards bulk results.

1. INTRODUCTION

Indentation tests, in many cases referred to as hardness tests, have for a long time been a standard method for material characterization as they provide a convenient, non-destructive, experimental method for evaluating basic properties from small samples of material. The advantage, in comparison with a uniaxial tensile test, is of course the relative simplicity of the experimental setup. On the other hand, an obvious drawback is the very complicated mechanical problem arising owing to inhomogeneous deformation in the indented materials. Therefore, until recently the interpretation of indentation tests has relied heavily on semiempirical formulae, the work by Tabor (1951) is perhaps the best example of this, with no or little theoretical foundation. With the advent of modern computers and advanced numerical methods, however, the understanding of the mechanics involved during ball indentation (Hill *et al.*, 1989; Kral *et al.*, 1993; Storåkers and Larsson, 1994), cone indentation (Laursen and Simo, 1992), and Vickers indentation (Giannakopoulos *et al.*, 1994), has increased rapidly in recent years. This new interest in the mechanical behaviour of indentation testing is to a large extent a result of the increased use of new materials such as ceramics and composites in structural and other devices. These materials are notoriously difficult to characterize through uniaxial or other standard tests which in many cases make indentation testing the only possible alternative for determining their mechanical properties (Rowcliffe, 1991).

During the last decade a new generation of indentation devices, so-called ultra-low load or depth-sensing indentation systems [see for example Pethica *et al.* (1983) and Loubet *et al.* (1984)], have been developed in order to make possible *in situ* testing of mechanical properties of materials, such as thin coatings (Söderlund *et al.*, 1994). Even more important are the new possibilities for quantitative determination of several important mechanical properties in addition to hardness. This arises due to the continuous recording of both load and displacement during the entire indentation cycle. In the ultra-low indentation experiments a three-sided pyramidal indenter (a Berkovich) most often is used, since the

†Author to whom correspondence should be addressed.

geometry is easier to fabricate with a sharp tip than the Vickers indenter is. The inclined angle of the Berkovich indenter (24.7°) has been chosen in order to obtain the same area to depth characteristics as the Vickers indenter has. Numerous papers deal with depth-sensing indentation experiments, which relay on Berkovich indentation (Pethica *et al.*, 1983; Loubet *et al.*, 1984; Söderlund *et al.*, 1994; Doerner and Nix, 1986; Mayo and Nix, 1988; Mayo *et al.*, 1990; Oliver and Pharr, 1990). A corresponding theoretical analysis is, however, almost completely lacking.

We have been able to find two references, Barber and Billings (1990) and Bilodeau (1992), presenting an approximate solution for Berkovich indentation of linear elastic materials while, to our knowledge, the corresponding problem of elastoplastic indentation has been left completely untouched by the scientific community. It is, therefore, the aim of the present paper to analyse, using numerical methods, the mechanics involved at Berkovich indentation of elastic materials and metals and to compare these theoretical findings with carefully designed nano- and microindentation experiments. Special attention will also be given to the following issues: (1) the validity of well known formulae for determining elastic material constants during unloading. (2) The effect of large rotations on the results. (3) An overall comparison between the characteristics of Vickers, Giannakopoulos *et al.* (1994), and Berkovich indentation. As a result of this analysis, universal formulae for hardness and the load–indentation depth relation will be presented. Owing to the complexity of the problem, which is unavoidably three-dimensional, the numerical analysis will be performed using the finite element method. In the experimental part of the investigation both nano- and microindentation were carried out in order to obtain indentations of a wide range of sizes.

2. BASIC EQUATIONS

The geometry of the Berkovich indentation test is shown schematically in Fig. 1. Basically we attack the mechanical problem resulting when a rigid indenter is pressed into a homogeneous, isotropic and semi-infinite body. Indentation is considered to take place under quasi-static and isothermal conditions. Furthermore, bulk constitutive behaviour is assumed for the indented material which essentially means that the derived results are meaningful only when the indentation depth is much greater than the characteristic microstructural size of the indented material.

With these basic assumptions in mind, and within a small strain formulation of the problem, linear elastic materials are described constitutively by Hooke's law as

$$\sigma_{ij} = \frac{E}{1+\nu}\left[\delta_{ik}\delta_{jl} + \frac{\nu}{1-2\nu}\delta_{ij}\delta_{kl}\right]\varepsilon_{kl}, \tag{1}$$

where in ordinary notation σ_{ij} is the Cauchy stress, E (>0) is the Young's modulus, ν ($-1 < \nu < 0.5$) is the Poisson's ratio, δ_{ij} is the Kroneckers identity tensor and ε_{kl} is the small strain tensor.

At incremental, rate-independent, elastoplastic material behaviour, eqn (1) must be replaced by the Prandtl–Reuss equations reading

$$\dot{\sigma}_{ij} = \frac{E}{1+\nu}\left\{\delta_{ik}\delta_{jl} + \frac{\nu}{1-2\nu}\delta_{ij}\delta_{kl} - \frac{3\sigma'_{ij}\sigma'_{kl}E/(1+\nu)}{2\sigma_e^2\left(\frac{2}{3}H + \frac{E}{1+\nu}\right)}\right\}\dot{\varepsilon}_{kl}. \tag{2}$$

In eqn (2), $H(=\mathrm{d}\sigma/\mathrm{d}\varepsilon_p)$ is the instantaneous slope of the uniaxial nominal stress, σ, vs the engineering (nominal) plastic strain, $\varepsilon_p = \varepsilon - \sigma/E$, given from a simple uniaxial compression test ($\sigma = \sigma(\varepsilon)$). The dot superscript indicates time variation. Furthermore, $\sigma_e = (\frac{3}{2}\sigma'_{ij}\sigma'_{ij})^{1/2}$ is the effective stress according to von Mises and $\sigma'_{ij} = \sigma_{ij} - \sigma_{kk}\delta_{ij}/3$ is the deviatoric stress.

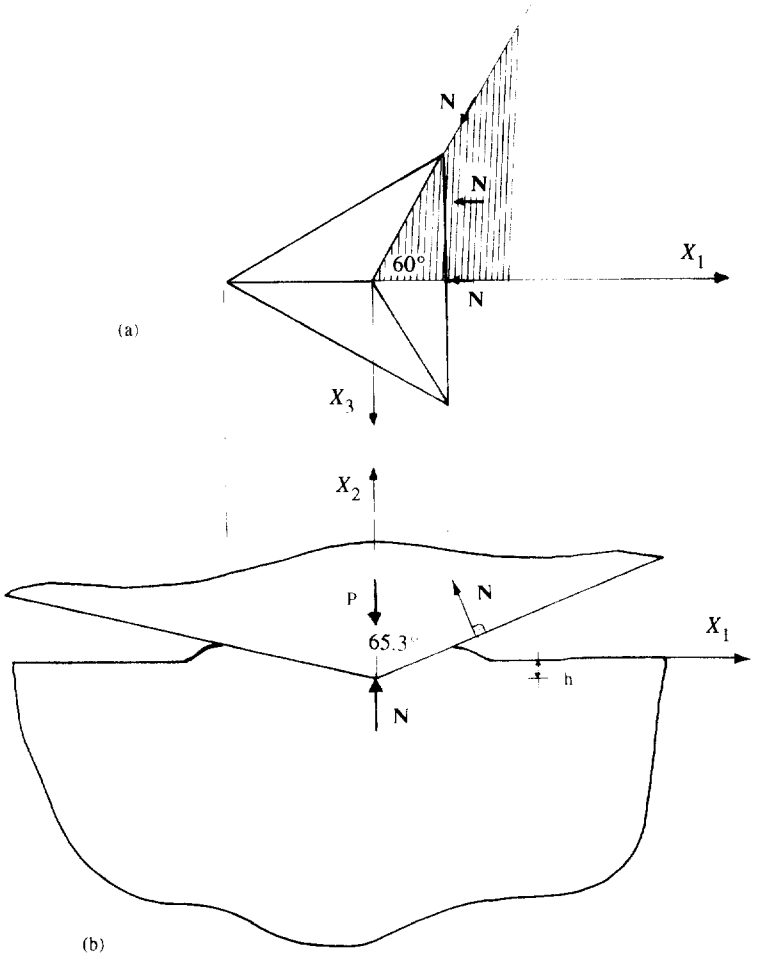

Fig. 1. Schematic of the geometry of the Berkovich test. (a) Top view. (b) Side view.

At incremental elastoplastic deformation, the accumulation of total plastic strain is given by

$$\varepsilon_p = \int_0^t \left(\frac{2}{3}\dot{e}_{ij}\dot{e}_{ij}\right)^{1/2} \mathrm{d}t. \tag{3}$$

It should be emphasized that eqn (2) is only valid at plastic loading when $\sigma_e = \sigma(\varepsilon_p)$ (the initial yield stress is given by $\sigma_y = \sigma(0)$). At elastic loading or unloading, eqn (1) must be used, formulated in incremental form.

Within linear kinematics, the strain tensor, ε_{ij}, is connected with the displacements, u_i, as

$$\varepsilon_{ij} = (\partial u_i/\partial X_j + \partial u_j/\partial X_i)/2, \tag{4}$$

where partial differentiation is with respect to the reference fixed Cartesian system X_i. In absence of body and inertia forces, the equilibrium equations to be satisfied read

$$\frac{\partial \sigma_{ij}}{\partial X_j} = 0 \tag{5}$$

Together with the boundary conditions, to be specified later, eqns (1)–(5) fully describe,

within a small strain formulation, the elastic and elastoplastic boundary value problems presently under investigation.

Giannakopoulos *et al.* (1994), in their numerical analysis of the Vickers indentation test, concluded that the essential parameters of the problem were well captured within a small strain formulation of the problem. Presently, with an inclined angle of 24.7°, compared to 22° at Vickers indentation, even larger rotations are enforced at the contact area and it seems advisable also in this case to compare the small strain results with corresponding ones derived using a large strain formulation. To this end, essentially the same observation as by Giannakopoulos *et al.* (1994) was made as the rate of rotation of the principal axes of deformation equals the rate of rigid body rotation, a hypoelastic formulation of Hooke's law was relied upon yielding

$$\hat{\tau}_{ij} = \frac{E}{1+\nu}\left[\delta_{ik}\delta_{jl} + \frac{\nu}{1-2\nu}\delta_{ij}\delta_{kl}\right]D_{kl}. \tag{6}$$

For elastoplastic deformation the large strain formulation of Prandtl–Reuss equations reads

$$\hat{\tau}_{ij} = \frac{E}{1+\nu}\left(\delta_{ik}\delta_{jl} + \frac{\nu}{1-2\nu}\delta_{ij}\delta_{kl} - \frac{3\tau'_{ij}\tau'_{kl}E/(1+\nu)}{2\tau_e^2\left(\frac{2}{3}H + \frac{E}{1+\nu}\right)}\right)D_{kl}. \tag{7}$$

In eqns (6) and (7), D_{ij} is the rate of deformation and $\hat{\tau}_{ij}$ is the Jaumann rate of the Kirchhoff stress, τ_{ij}, related to the Cauchy stress as $\tau_{ij} = J\sigma_{ij}$ where J is the determinant of the deformation gradient tensor. τ_e and τ'_{ij} being Mises effective stress and the deviatoric stress respectively, defined as in the small strain formulation of the problem. Furthermore, in eqn (7) $H(= \mathrm{d}\tau/\mathrm{d}\varepsilon_{ip})$ is the instantaneous slope of the uniaxial compressive Kirchhoff stress, τ, vs the logarithmic accumulated plastic strain, ε_{ip}, defined in accordance with eqn (3). As in the small strain analysis, the elastoplastic constitutive specification, eqn (7), is only valid at plastic loading when $\tau_e = \tau(\varepsilon_{ip})$ (the initial yield stress is given by $\tau_y = \tau(0)$). At elastic loading or unloading, eqn (6) holds.

To sum up the governing equations, in the large strain formulation, D_{ij}, is connected with the material velocity, $\dot{u}_i$, as

$$D_{ij} = (\partial \dot{u}_i/\partial x_j + \partial \dot{u}_j/\partial x_i)/2, \tag{8}$$

x_i being the current position of a material point initially at X_i, and in absence of body and inertia forces the equilibrium equations to be satisfied are

$$\frac{\partial \sigma_{ij}}{\partial x_j} = 0. \tag{9}$$

As regards boundary conditions, the surface of the half-space outside the contact area is assumed traction free and as a result

$$\sigma_{1j}n_j = \sigma_{2j}n_j = 0 \tag{10a}$$

$$\sigma_{3j}n_j = 0. \tag{10b}$$

where n_i is the outward unit normal vector of the half space (defined in the deformed configuration at large strain analysis). Presently, no friction is considered between the indenter and the material, and as a consequence, eqn (10a) still holds at the contact area while eqn (10b) is formally replaced by unilateral kinematic constraints given by the shape of the Berkovich indenter as shown in Fig. 1.

3. NUMERICAL ANALYSIS

The boundary value problems presented in the previous section are fundamentally very difficult to attack for a number of reasons. Not only are they unavoidably three-dimensional, but they also involve material and geometrical nonlinearities as well as a contact problem with a moving contact boundary. Therefore, numerics have to be relied upon extensively and in particular the finite element method. To this end, the ABAQUS general purpose program (1992) proved advantageous to use. Furthermore, remembering the similar features involved at Vickers and Berkovich indentation basically the same numerical considerations need to be addressed when analysing the mechanical behaviour of the two hardness tests. With this in mind, we followed the numerical approach developed by Giannakopoulos *et al.* (1994) in their analysis of the Vickers hardness test regarding such features as meshing, integration, numerical testing, far-field boundary conditions and contact analysis.

One of the main differences, regarding geometrical considerations, between the present analysis and the one performed by Giannakopoulos *et al.* (1994) is the symmetry involved in the problem. As depicted in Fig. 1a, the symmetry at Berkovich indentation is six-fold, only one sixth of the body needs to be modelled, while an eight-fold symmetry is present at Vickers indentation. In order then to retain the numerical accuracy achieved by Giannakopoulos *et al.* (1994), more elements were required when discretizising the half-space. The resulting finite element mesh used in the elastoplastic analysis is depicted in Fig. 2 which consists of 10,850 eight-noded isoparametric block elements and 12,400 nodes. This compares with 9914 nodes and 8524 eight-noded elements needed in the analysis of the Vickers test (Giannakopoulos *et al.* 1994). Inside each element, the displacements were approximated using trilinear shape functions. In relation to Fig. 2a, the indented body is bounded by five characteristic surfaces I–V. The plane I is the indented surface with the contact elements, the cylindrical surface V is traction free and the planes II–IV can only deform in their own planes. Owing to the severe nonlinearities present in the problem, loading had to be applied stepwise. This procedure was then continued until steady-state conditions were found for the load–indentation depth relation and the hardness, as well as steady-state shapes for stress and strain isocontours. In all calculations, this required a contact area between the indenter and the material that was resolved by at least 50 elements.

Formally, the indentation load was given by

$$P = -\int_{\Gamma_c} \sigma_{ij} N_j \, \mathrm{d}\Gamma_c \tag{11}$$

where Γ_c is the actual area of contact and N_j is the inward unit normal vector to the rigid surface of the indenter. The average pressure is then calculated directly, using the projected contact area A_p, as

$$p_m = P/A_p = P/(\Gamma_c \cos 24.7^\circ). \tag{12}$$

It remains then to specify the materials used in the numerical analysis. For the elastic calculations, we constantly used the value 2.1×10^{11} Pa for Young's modulus E, noting that E in this case is only a scaling factor, while Poisson's ratio was given values between 0 and 0.5. For the small strain elastoplastic calculations basically the same materials as the ones considered by Giannakopoulos *et al.* (1994) were analysed, namely aluminium 7075-T6 and 6061-T6. These materials are common rate-independent construction materials and well characterized in compression by Maiden and Green (1966) for plastic strains up to 6 and 7.5%, respectively. At higher strains, for reasons of generality (through parametric study) of the results, we considered different types of hardening. The small strain constitutive characteristics of the materials analysed are depicted in Fig. 3 where materials A and B correspond to no plastic hardening at high strains, while linear hardening is represented by materials C and D. For materials with no hardening at high strains, the ultimate stress will be denoted σ_u. For the large strain elastoplastic calculations we used the constitutive

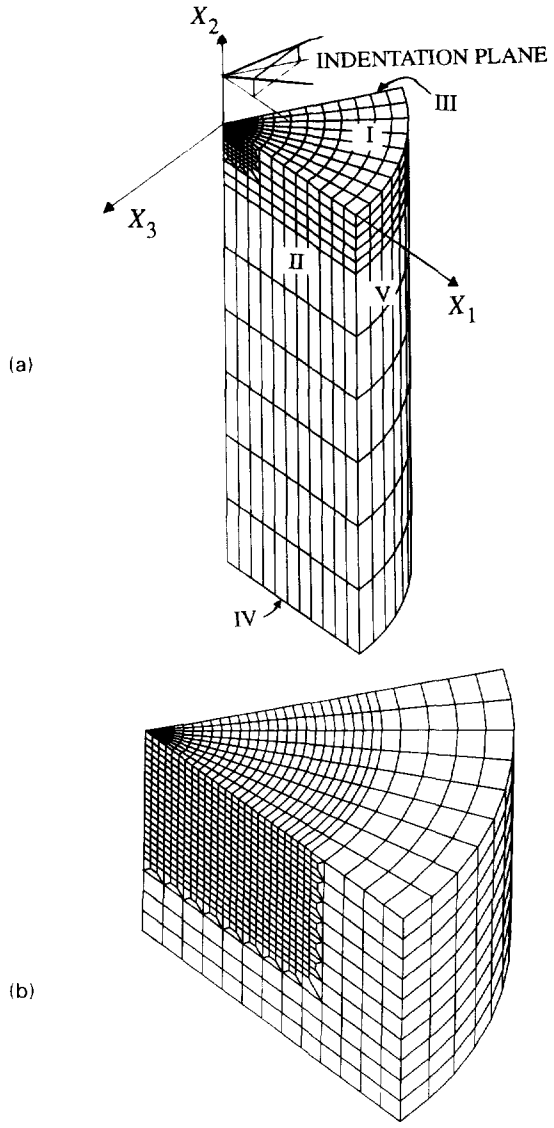

Fig. 2. The FEM mesh used in the numerical calculations. (a) General view. (b) Detail of the mesh at the region of contact. 10,850 eight-noded elements (12,400 nodes).

characteristics of material C, 7075-T6 with linear hardening. In this case, however, the nominal uniaxial compression curves in Fig. 3 had to be translated to the true stress vs logarithmic strain curves by the relations $\tau = \sigma(1-\varepsilon_p)$ and $\varepsilon_{lp} = -\ln(1-\varepsilon_p)$. As a final comment it should be emphasized that both uniaxial tensile tests on 7075-T6, Hallbäck (1993), and presently performed uniaxial compression tests on 6061-T6 indicated very close to nominal linear hardening at large strains. For this reason, only materials C and D in Fig. 3, representing the actual nominal compression tests of Al 7075-T6 and 6061-T6 respectively, will be used for comparison with experimentally determined hardnesses.

4. EXPERIMENTAL APPROACH

The materials indented were Al 6061-T6 and Al 7075-T6. As mentioned earlier both uniaxial tensile and compressive tests were carried out on these materials in order to fully describe the plastic hardening present at high strains. The materials were polished and etched in order to measure the grainsizes. Both materials showed elongated grains. The grain size in the rolling direction was approximately 350 μm, and 15 μm in the perpendicular

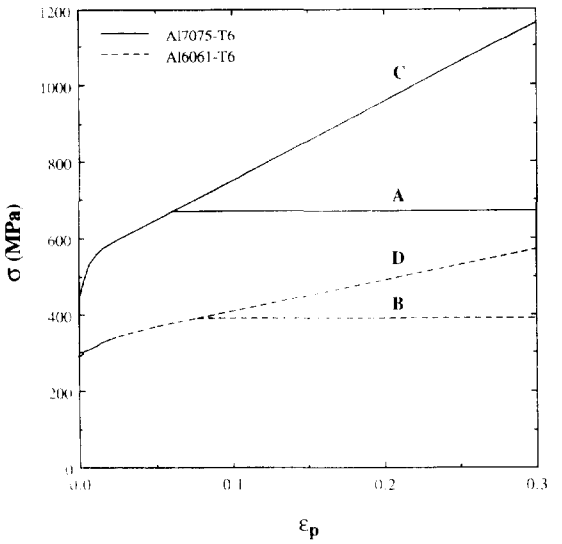

Material	E (GPa)	ν	σ_y	σ_u
7075-T6	72	0.28	415.7	669.8
6061-T6	70	0.28	287.4	317.6

Fig. 3. Uniaxial nominal compression curves for the materials used in the numerical calculations.

direction. This microstructure creates some slight elastic and plastic anisotropy. The indentation tests were, therefore, performed in different orientations in order to average out the grain anisotropy. Of course, for materials exhibiting strong elasto-plastic anisotropy we expect a pronounced influence of it on the indentation deformation (the stiffer direction being less deformed), resulting in a very unsymmetric residual imprint. Such imprints were not found from the present levels of indentation of the particular aluminium alloys tested. At extremely small indentations, nanoindentation, all experiments were performed in individual grains but the results seemed independent of the grain size effect. This indicates that the grain boundaries do not act very differently from the interior grains under the present deformation pattern. Also, the development of slip lines is relatively easy and in many directions (Al is face-centered cubic) to ensure the validity of classic Mises elastoplastic modelling. Before performing the indentation experiments, the specimens were mechanically polished with subsequently finer diamond slurries down to 1 μm. The final polishing was made with 0.04 μm colloidal silica in order to reduce further the surface damage.

The indentations were made with a depth-sensing indentation system (Nanoindenter I, Nano Instruments Inc., Knoxville, TN, U.S.A.) equipped with a Berkovich indenter, as well as by using a universal testing machine (Model 1361, Instron Corp., High Wycombe, U.K.) equipped with Berkovich and Vickers indenters. The loads used in the ultra-low load indentation experiments were 100, 75, 50, 25 and 10 mN, respectively. The corresponding loading rates were chosen to give a loading and unloading time of 33 s, respectively. At maximum applied load a dwell time of 20 s was inserted to achieve equilibrium and to get a more well defined slope of unloading. At 90% of the unloading another dwell time of 20 s was implemented to check and compensate for the thermal drift in the system. Loads of 10, 15, 25, 500 and 1000 N, respectively, were used for Vickers indentation. An indentation load of 25 N proved to be the upper limit due to the dimensions of the Berkovich indenter presently used. The loading and unloading rates were again chosen as to give a loading and unloading time of 33 s, respectively. A 20 s dwell time was applied at maximum loading for the Vickers indentation as well. For each load, material and indenter geometry approximately 10 indentations were made. The diamond holder and the specimen support were carefully designed to minimize the indenter system compliance. Continuous load–displacement curves were recorded for all indentations.

The data obtained from the Instron machine were corrected for the additional machine complience and for the zero-offset in displacement. The zero-offset was found by fitting the loading curve to a perfect quadratic polynomial. The hardness at maximum load was calculated using the relation $H = P/(24.56h^2)$ for the Berkovich indenter and $H = P/(24.50h^2)$ for the Vickers indenter, i.e. by assuming ideal tip geometries and neglecting the effect of piling-up and sinking-in along the contact boundary. It should be pointed out here that as continuous load–displacement curves were recorded during all experiments the value of h, the indentation depth, used when evaluating the experimental results was, indeed, the true total depth including both elastic and plastic contributions. Hardness numbers were also derived from optically measured values of the real projected contact area, including irregularities, using an image processing system (Quantimet 500, Leica Cambridge Ltd, Cambridge, U.K.), as well as in the traditional way from recovered side lengths, L, by assuming a perfect equilateral triangle, $A = \sqrt{3}L^2/4$. The elastic stiffness was calculated using the solution to the elastic punch problem by assuming flat punch geometry.

$$E(1-\nu^2) = \frac{\mathrm{d}P}{\mathrm{d}h}\left(C\sqrt{A_{\max}}\right),$$

where, according to King (1987), C is 1.167 for the Berkovich and 1.142 for the Vickers geometries, respectively. The stiffness $\mathrm{d}P/\mathrm{d}h$ was calculated from the first third of the unloading as previously suggested by Doerner and Nix (1986) and Oliver and Pharr (1992) as well as from the first tenth of the unloading force–depth curve.

5. RESULTS AND DISCUSSION

In the following, the numerical and experimental results presently derived will be presented in detail and compared with pertinent results from earlier analysis, in particular with similar results derived by Giannakopoulos *et al.* (1994) (GLV) relating to the Vickers hardness test. The results presented below, for elastic and elastoplastic indentation, include: (1) bulk results featuring load–indentation depth relations and hardness formulae, (2) local results featuring the deformation mode at the contact boundary and the shape of the contact area, (3) isocontours for different field variables (Cauchy stress invariants and accumulated effective plastic strain). In the elastic case a somewhat detailed consideration of the stress singularities will be presented while characteristics of the initial loading curve and the size of the plastic zone will be commented upon when dealing with elastoplastic materials. Furthermore, similarities and differences, between small strain and large strain results will be exemplified and properly addressed.

5.1. *Elastic case*

Judging from the stress levels presented below, purely elastic indentation of materials with idealy sharp indenters is very hard, if not impossible, to achieve in practice. Having said that, however, we still believe that elasticity can be of interest in some particular cases. There do exist materials for which the elastic results derived here can be pertinent, for example cellular solids (Gibson and Ashby, 1988), and rubbers. The elastic results can, of course, also serve as a numerical guideline for other investigations.

In the Berkovich indentation test, as presently stated, the indentation depth, h, is the only characteristic length of the problem. Dimensional considerations then indicate that the average pressure between the indenter and the material must be constant throughout an indentation test. We performed a number of calculations for different values on h and Poissons ratio ν (ν was varied between 0 and 0.5) and found numerically, by curve fitting, the relationship

$$p_c = 0.2201(1 - 0.21\nu - 0.01\nu^2 - 0.41\nu^3)\frac{E}{1-\nu^2} \tag{13}$$

for the small strain solution. Obviously a constant value on the contact pressure indicates, by geometrical arguments, a parabolic relationship between the total load P and the indentation depth h. Indeed, this was also found numerically reading

$$P = 2.1891(1 - 0.21\nu - 0.01\nu^2 - 0.41\nu^3)\frac{E}{1-\nu^2}h^2. \tag{14}$$

When comparing the results from eqns (13) and (14) with corresponding ones derived using a large strain hypoelastic formulation of the governing equations, very small differences were found. In fact, the total load at a given value on h proved to be exactly the same while the average pressure was somewhat lower, 4.8%, in the large strain solution. The large strain average pressure results for the Vickers test were only 0.1% lower.

As already discussed, experimental verification of eqns (13) and (14) cannot be found in the literature as Berkovich indentation of metals undoubtedly includes plastic effects even at small indentations. Some previous theoretical results by Barber and Billings (1990) and Bilodeau (1992) are, however, relevant for a comparison. It should be remembered though that these authors do not correctly describe the influence of Poisson's ratio in their calculations which essentially enters their equations only through $E/(1-\nu^2)$ and, therefore, a direct comparison between our and their results is not possible to perform. However, the reported results by Barber and Billings (1990) where only total indentation load was calculated, and by Bilodeau (1992) where both total indentation load and average constant pressure were calculated, are within the range of eqns (13) and (14) when ν varied between 0.0 and 0.5.

Some comparison with GLV results for the Vickers hardness test also seems to be in order. Explicit calculations of the total load and the contact pressure, for the same indentation depth, then reveal a very close agreement between the results derived for the two indenters, with Berkovich values being slightly higher, but less than 5%. This is in accordance with expectations remembering that the Berkovich indenter has been designed in such a way that it would include the basic features of a Vickers indentation test.

Next we turn our attention to explicit field results, and especially the stress invariants, as shown in Fig. 4. Here, both small (Fig. 4a) and large (Fig. 4b) strain results for the von Mises effective stress as well as large strain results for the hydrostatic stress (Fig. 4c) are depicted. Quite clearly the large and small strain isocontours are very similar, which is somewhat surprising considering the high strains (> 70%) involved. The similarities with the Vickers fields, as presented by GLV, are also obvious although a close inspection of the isocontours indicates more pronounced stress singularities at Berkovich indentation. A detailed analysis of the second Piola–Kirchoff contact tractions, S_{22}, shows that, for small strains and $\nu = 0.3$, they can be asymptotically approximated as

$$S_{22}(1-\nu^2)/E = -0.2503\ln(r/h)\left(\frac{r}{\phi + \pi/3}\right), \quad r \to 0, \quad \phi \to -\pi/3, \tag{15}$$

where $r^2 = X_1^2 + X_2^2$ and $\tan\phi = X_2/X_1$. The range of validity for eqn (15) is $r < h/2$ and $-\pi/3 < \phi < -0.92(\pi/3)$. In the Vickers analysis, GLV, the singularity in the ϕ-direction was found considerably weaker, in fact it was logarithmic. This finding is in some accord with results by Dukino and Swain (1992) who found the Berkovich test more favourable when crack initiation and growth was warranted, although it should be underlined that those results are strictly valid only for ceramics. Regarding the singularities present in the large strain analysis, these can actually be determined analytically using the results by Williams (1952) which give a stress singularity of $r^{-0.545}$ in the radial direction, r being the distance from the edge in the deformed configuration. This is stronger than what was found

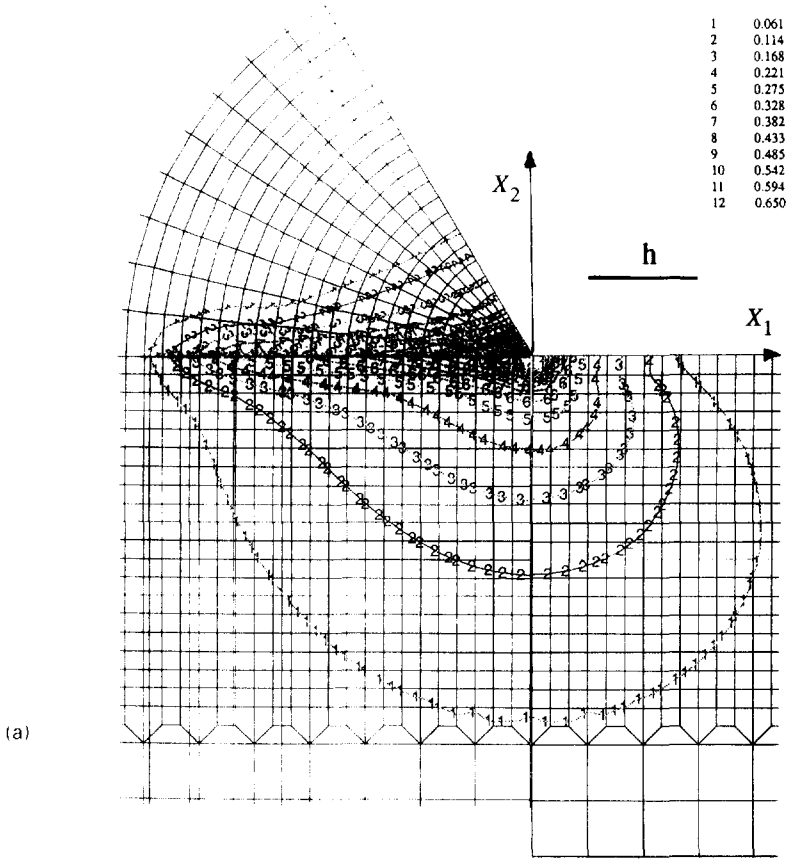

Fig. 4. Stress invariants for the elastic case. The stresses are normalized by $E/(1-\nu^2)$. The indentation depth h is also shown. $\nu = 0.3$. (a) Mises effective stress (small strain results). (b) Mises effective stress (large strain results). The deformation is also shown. (c) Hydrostatic stress (large strain results). The deformation is also shown. (*Continued opposite and overleaf.*)

for elastic Vickers indentation, $r^{-0.337}$, and is due to the smaller dihedral angle present at Berkovich indentation. Numerically, we found the stress singularity to be $r^{-0.294}$ with range of validity $r < h/2$.

The contact area, in the small strain solution, differs substantially from a triangle. For $0 \leqslant \nu \leqslant 0.5$, the projected contact contours were found numerically by curve fitting to be parts of hyperbolas that followed, within 4% accuracy, the relation

$$\left(\frac{X_1}{1.18h}\right)^2 - \left(\frac{X_2}{2.70h}\right)^2 = 1. \tag{16}$$

Comparison of eqn (16) with the boundary element results by Barber and Billings (1990) shows very good agreement, within 1.3%, while Bilodeau's (1992) assumption of a triangular contact area renders a direct comparison with the present results irrelevant. For the large strain solution the contact area proved to be slightly larger (5%) but with the same shape as in the small strain solution. Note that the large strain results for the Vickers test showed a contact area almost the same as for the small strain results.

Finally, the deformation field depicted in Fig. 4b (and in Fig 4c) deserves some comments. In all elastic calculations, uneven material sinking-in occured at the contact contour. Furthermore, it is interesting to note the very small tangential displacements at the contact area. This feature of the solution is important as it, to some extent, justifies the present assumption that friction does not play a major role during the indentation process (at least not in the elastic case).

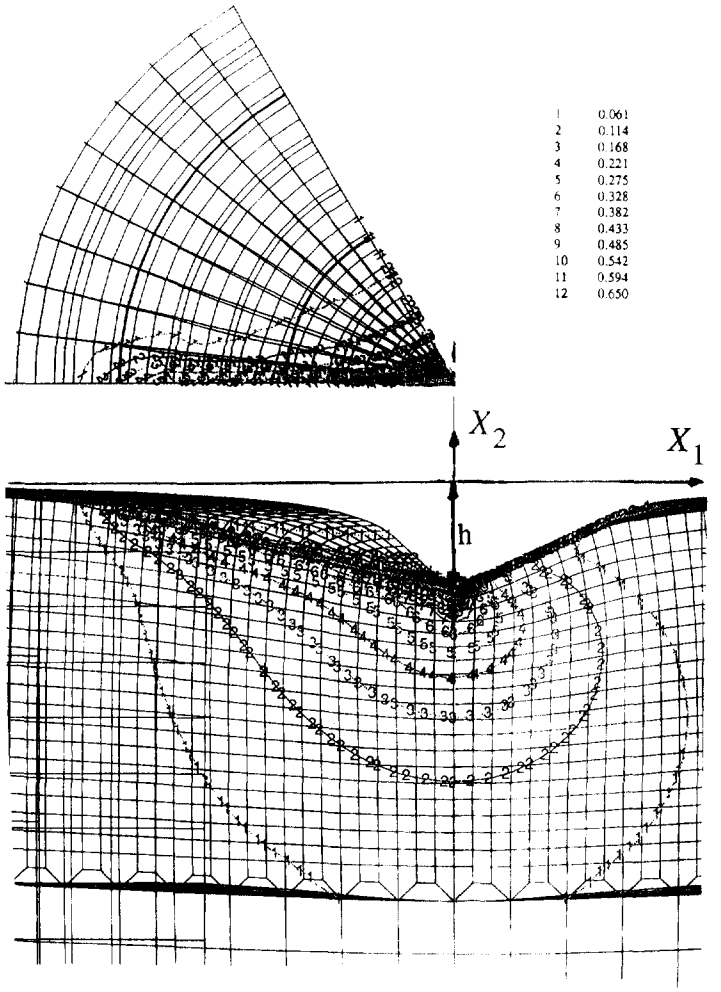

Fig. 4 (continued)

5.2. *Elastoplastic case*

Depth-sensing indentation can be a very useful tool for determining the constitutive behaviour of the indented material. Basically, the material parameters pertinent to plasticity are determined during the loading process by examining the hardness, here defined as the average pressure at maximum load, and the relation between the total load and the indentation depth, while the elastic stiffness is given by the initial slope of the unloading curve. Furthermore, the mechanical fields involved are also of definite interest as they can provide important information related to, for example, crack formation and growth.

The size and shape of the contact area is of fundamental importance when analysing, both numerically and experimentally, an indentation test. It, therefore, seems natural to start the presentation of the results by discussing this parameter. For this purpose the contact area at Berkovich indentation, in the undeformed configuration, is shown in Fig. 5a for aluminium 7075-T6 (material C1). As was the case for all materials analysed the contact area proved to be an almost perfect triangle in the undeformed (projected) configuration. However, a close inspection of the displacement fields showed that the displacement in the X_1-direction, u_1, is unevenly distributed along the boundary of contact. Essentially u_1 takes on very small values along plane III (see Fig. 2a) resulting in a somewhat curved boundary of contact in the deformed configuration. Experimental evidence of this numerical finding is depicted in Fig. 5b, clearly showing the bulging of the contact boundary at the sides of the imprint. As a consequence of this effect the deformation mode changes from piling-up at the center of the edges (side II) to sinking-in near the corners (plane III), determined by actual value of the displacement u_3 at the contact boundary, regardless of

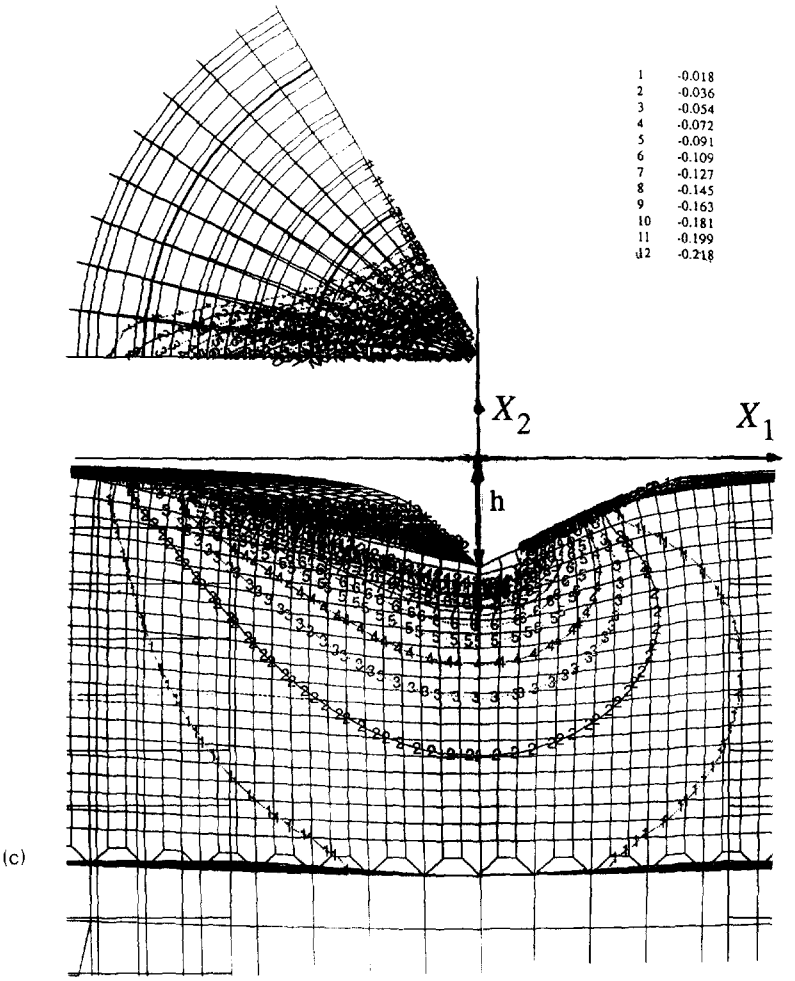

Fig. 4. *Continued*

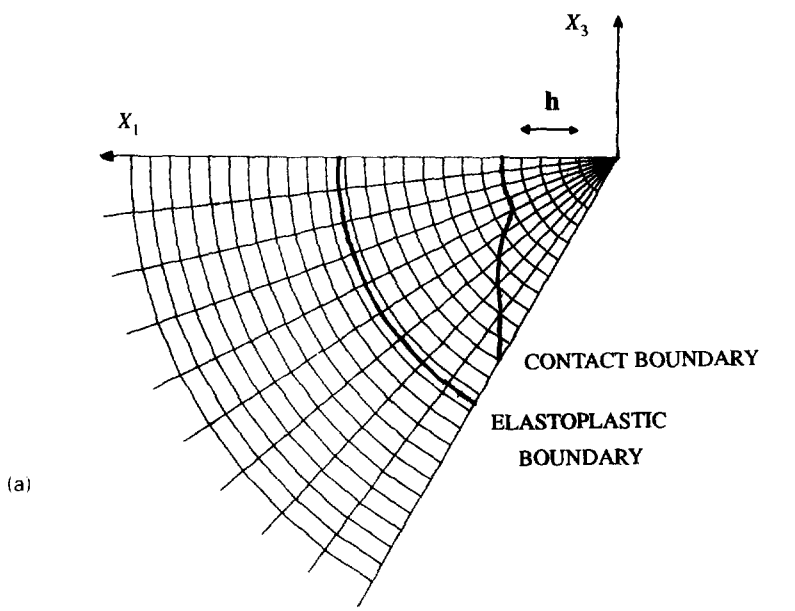

Fig. 5. Contact area and elastoplastic boundary as viewed from the surface for aluminium 7075-T6 (material C) at maximum load. The indentation depth h is also shown. (a) Small strain numerical results (in the undeformed configuration). (b) Typical experimental result for Berkovich indentation. (c) Typical experimental result for Vickers indentation. (*Continued opposite.*)

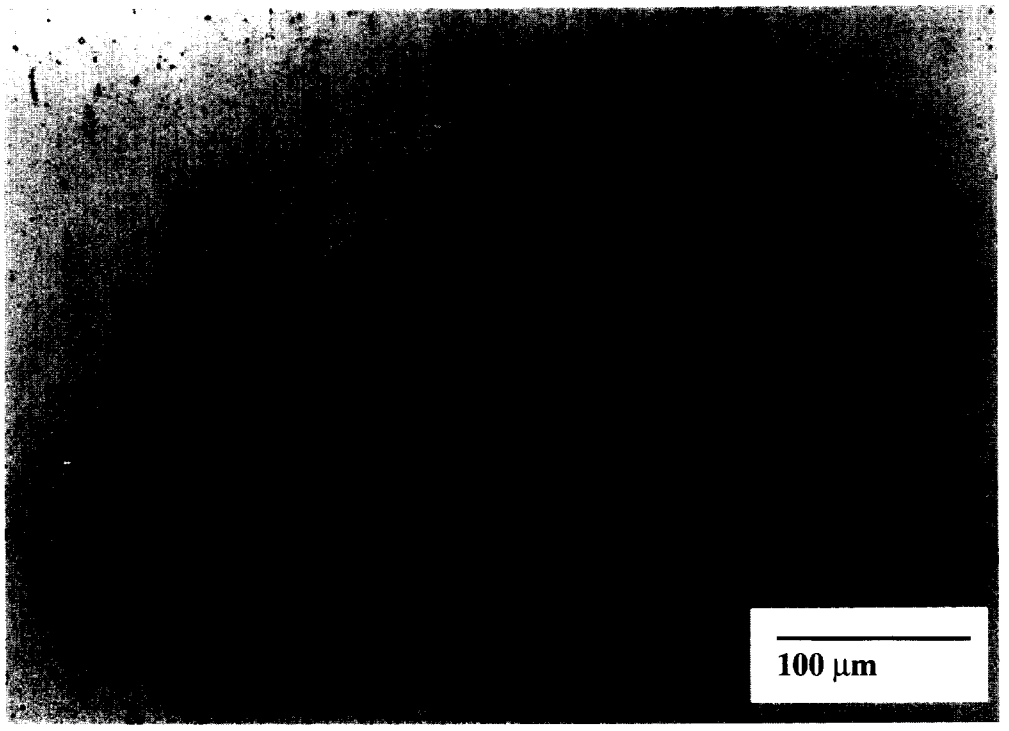

(b)

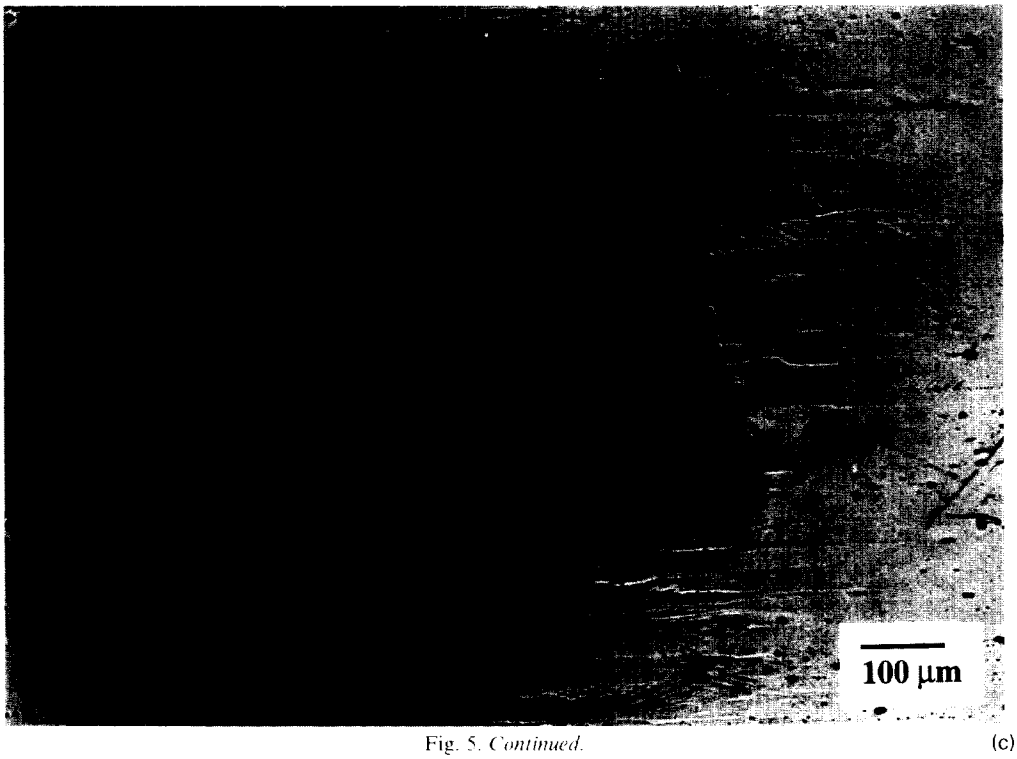

Fig. 5. *Continued.* (c)

the material characteristics (pile-up was, however, somewhat surpressed in the presence of plastic strain hardening). It should be pointed out that the deformation fields discussed above are shown indirectly in Figs 7b, 8b and 9b as the stress and strain fields given by the large strain formulation of the problem are presented in the deformed configuration (very little or no difference was found compared to the small strain results).

Fundamentally different results were found by GLV for the Vickers hardness test. In this case the contact area was almost a perfect square, both in the undeformed and in the deformed configuration. The square shape was verified experimentally as depicted in Fig. 5c. Naturally then, and in contrast to the Berkovich results, the deformation mode is the same all along the contact boundary but also very dependent on the type of hardening present at high strains.

The deformation in the Berkovich indentation, namely piling-up at the middle of the side and sinking-in at the corner, is an encouraging result as the contact area is then given by the idealized relation $A = 24.56h^2$ at maximum load, remembering that the effects of the two deformation modes cancel each other. Indeed, the numerically calculated contact areas were very close to this idealized relation for all materials investigated. This was also confirmed by the experiments. Figure 6a shows the hardness results for A17075-T6 and it is seen that the hardness calculated from the residual area (taking the bulging into account) almost equals the hardness obtained from the area derived at maximum load through the above mentioned area equation. Also note that these experimental hardness numbers are in excellent agreement with the hardness numbers obtained from the FEM calculations, which are based on the actual projected contact area at maximum load. On the contrary, the area calculated in the traditional way, from residual side length assuming a perfect equilateral triangle, strongly underestimates the contact area (since bulging is not accounted for) and thus gives rise to an overestimated hardness. Finally, it is seen in Fig. 6a that the indentations at indentation depths smaller than 1600 nm, in the nanoindentation regime, show a marked size effect, whereas the indentations deeper than 15.000 nm seem to be load independent. On the average the large indentations cover several grains, at least in one dimension, and the bulk constitutive behaviour can be considered closely fulfilled. Al 6061-T6 showed similar results, with a slightly larger difference, 4%, between the calculated hardness value and the hardness values derived from maximum depth and from the optically measured real residual area.

The numerical findings discussed above have important consequences when deriving a universal formula for the hardness as the effect of piling-up, or sinking-in, does not have to be addressed. Instead, essentially following the same arguments as GLV, we started from a semi-analytical expression by Johnson (1970), resting on the spherical cap approximation, and included the influence of the plastic hardening by a truncated power series. The outcome, derived from the small strain numerical results and for low strain hardening, reads

$$p_m = 0.245\sigma_r(1 + \sigma_r/\sigma)\left(1 - \ln\frac{E\tan 24.7^\circ}{3\sigma_r}\right). \tag{17}$$

In eqn (17) σ_r is the stress level at a plastic strain of 30% which could be characterized as a representative strain in the same way as in the Vickers test while the angle 24.7° is chosen in the spirit of Tabor (1951) due to the actual value of the inclined angle of a Berkovich indenter. Furthermore, through geometrical considerations and remembering the discussion above about the size and shape of the contact area, eqn (17) determines directly the corresponding formula for the total indentation load as

$$P = 1.273(\tan 24.7^\circ)^{-2}\sigma_r(1 + \sigma_r/\sigma)\left(1 + \ln\frac{E\tan 24.7^\circ}{3\sigma_r}\right)h^2. \tag{18}$$

The numerical accuracy of eqn (17) is shown in Fig. 6b, as for explicit numbers all calculated hardnesses and indentation loads fall within 5% of the ones given by eqns (17) and (18).

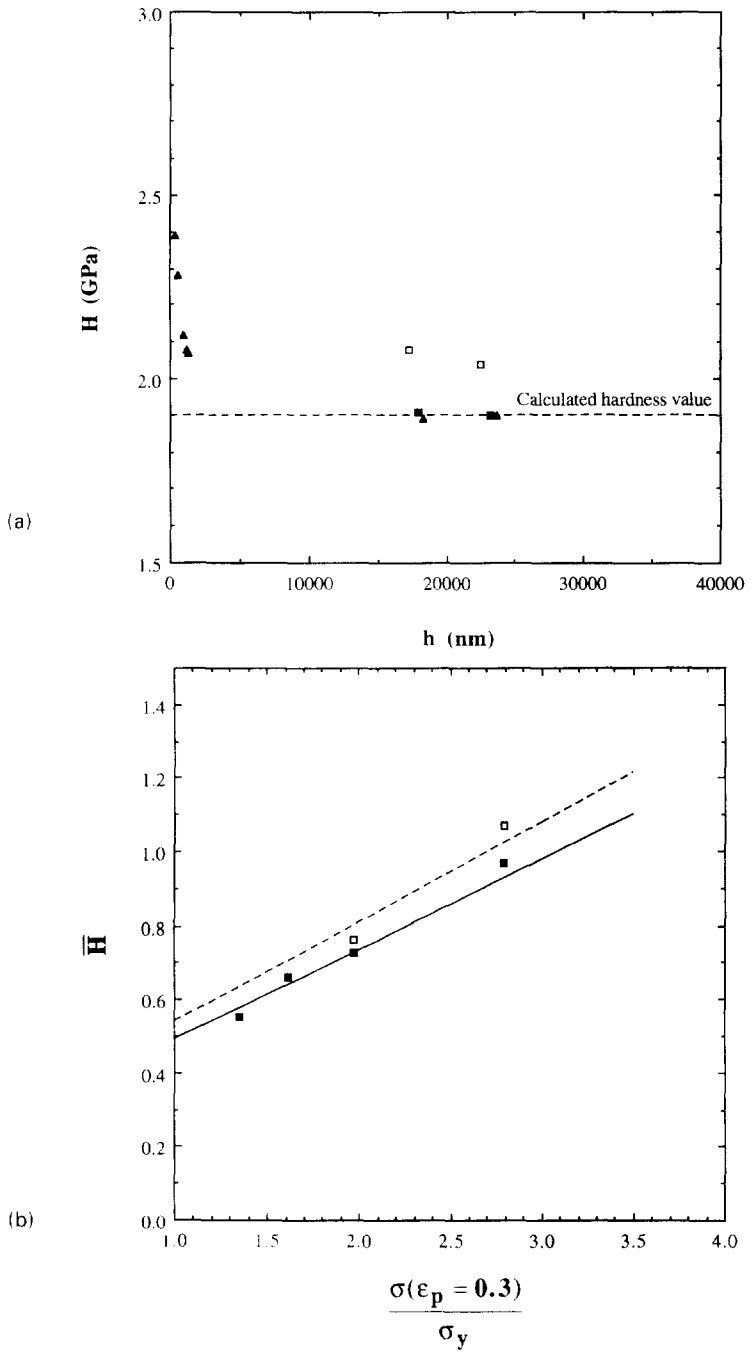

Fig. 6. Comparison between numerical and experimental results. (a) Hardness vs indentation depth for aluminium 7075-T6 (material C). (- - -) Large strain numerical result. (▲) Experimental results derived from the indentation depth. (■) Experimental results derived from the real projected residual contact area (measured optically). (□) Experimental results derived assuming the contact area to be a perfect triangle (side lengths measured optically). Each symbol represents five to 10 indentation experiments. (b) Normalized hardness, $\bar{H} = H/\sigma_y(1+\ln(E\tan 24.7^\circ/3\sigma_y))$ vs normalized uniaxial nominal stress, $\bar{\sigma} = \sigma(\varepsilon_p)\ \sigma_y$, at a plastic strain 0.3. (——), eqn (17). (- - -), eqn (17) scaled according to the large strain results (a factor of 1.1). (■) Small strain numerical results. (□) Experimental results. (c) Indentation load vs indentation depth for aluminium 7075-T6 (material C). (——), eqn (18) scaled according to the large strain results (a factor of 1.1). (+) Experimental results from the Instron general purpose testing machine. (d) Normalized indentation load, P/P_{max}, vs normalized indentation depth, h/h_{max}, for aluminium 7075-T6 (material C). (■) Large strain numerical results. (●) Experimental results from the nanoindenter, the maximum load ranged from 0.01 to 0.1 N. (*Continued opposite.*)

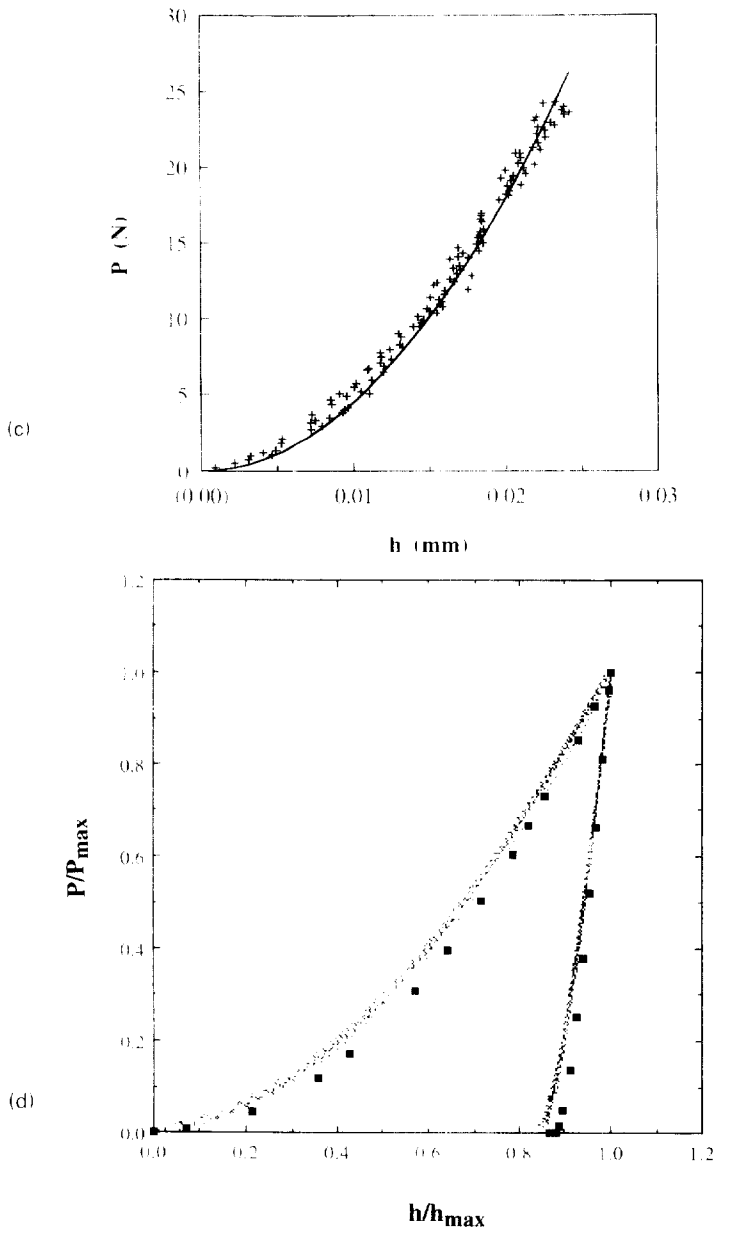

Fig. 6 (continued)

Further comparison with the large strain results, also presented in Fig. 6b, showed that the small strain calculations underestimate the total load by 10% while they correctly described the contact area. This is indeed surprising as the same 10% accuracy was found by GLV for the Vickers case using a completely different uniaxial stress–strain curve. This suggests that eqns (17) and (18) are valid also for a complete (large strain) description of the problem if they are appropriately scaled by a factor 1.1. This finding is also experimentally verified as depicted in Fig. 6b, and as discussed above for Fig. 6a, showing excellent agreement between the experimental results (steady state) and the scaled version of eqn (17).

In Fig. 6c, the large strain (scaled) version of eqn (18) is compared with the experimental results for aluminium 7075-T6 showing good agreement. Only the loading sequence is used for comparison though as again, in order to avoid indentation size effects, the experimental results were taken from the Instron machine at maximum indentation depths larger than 15 μm. The experimentally determined constant of proportionality between P

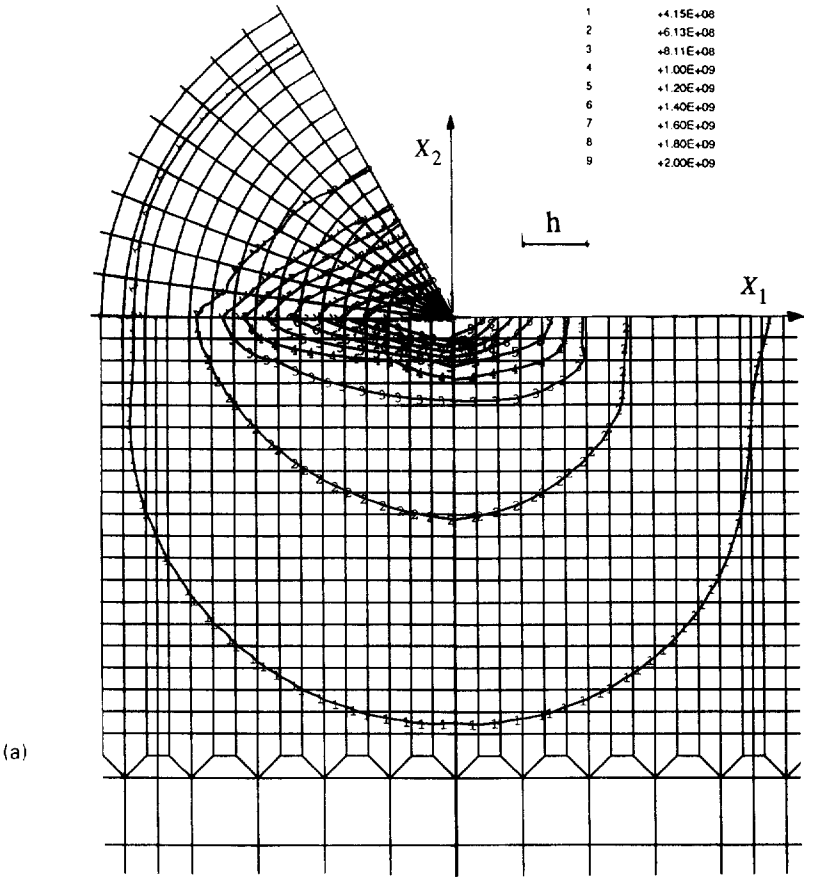

Fig. 7. Steady state von Mises effective stress for aluminium 7075-T6 (material C) at maximum load. Units are in Pa. The indentation depth h is also shown. (a) Small strain results. (b) Large strain results. The deformation is also shown. (*Continued opposite.*)

and h^2 showed large variations for individual indentations but the average of 15 indentations, $4.65 \pm 0.97 \times 10^{10}$, came close to the calculated value, 4.47×10^{10}. The variations are probably due to local fluctuations of the mechanical properties depending on grain orientation and the presence of microstructural features such as grain boundaries and defects.

The explicit results derived from eqns (17) and (18) proved to be very similar, within 5%, to corresponding ones presented by GLV for the Vickers hardness test. This was expected, as previously discussed, remembering that the Berkovich indenter was designed with the characteristics of the Vickers hardness test in mind. When inspecting our own and GLV results in some more detail we found that the Vickers hardness were slightly higher than the Berkovich ones for strain hardening materials while the opposite was found for materials with no strain hardening at high plastic strains.

The Instron machine proved, as also indicated by the scatter of experimental results in Fig. 6c, to be less accurate at unloading and in order to make an appropriate comparison between numerical and experimental results also in this case we used normalized nanoindentation curves (maximum load ranged from 0.01 to 0.1 N). The outcome is depicted in Fig. 6d. Obviously, the nanoindentation results differ somewhat from the numerical findings at loading. This can certainly be explained by the indentation size effect, an additional length (e.g. microstructure, surface effects, imperfectness of the diamond tip) enters the problem, discussed above. However, the normalization forces the two sets of results to coincide at the maximum load and we believe that at least for unloading the comparison is a proper one. Indeed, this assumption is verified by the experimental results in Fig. 6d where the different experimental curves almost coincide at unloading, indicating that the indentation size effect is much less pronounced at elastic deformation (no reverse plasticity

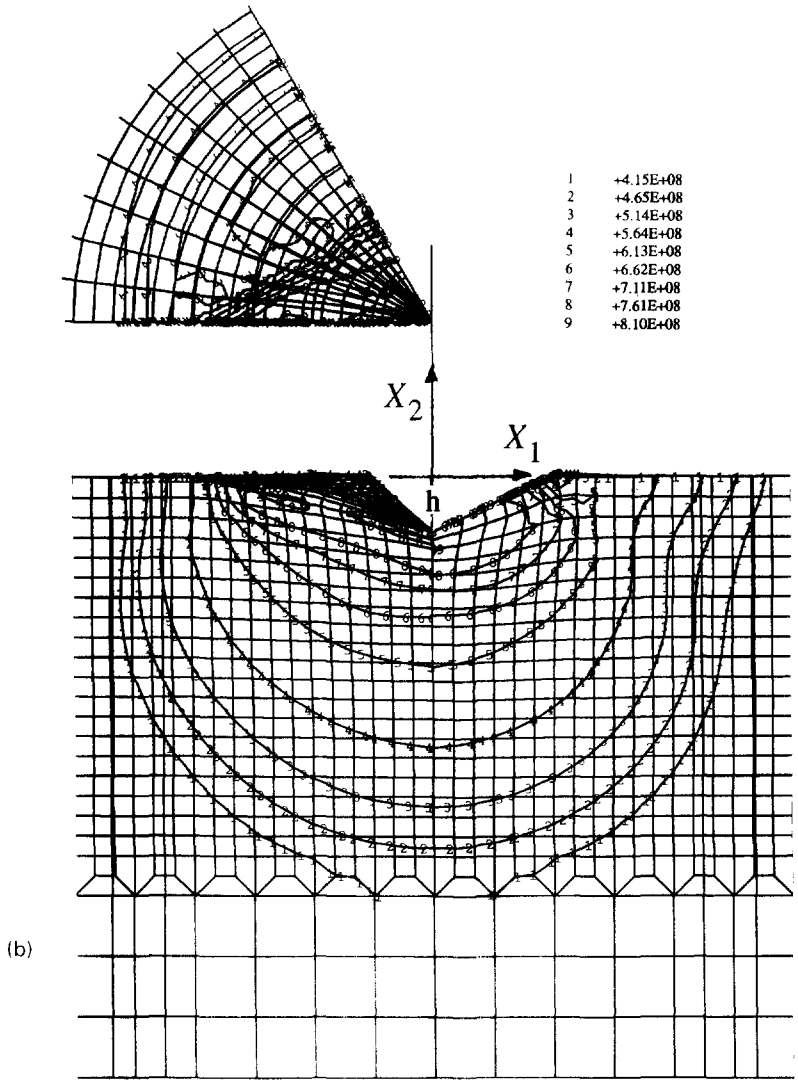

Fig. 7. (Continued)

occured during unloading). Clearly, according to Fig. 6d the numerically calculated loads are very similar to the experimental ones except close to complete unloading. The difference in the final indentation depth is, however, only 2% and remembering that the calculated unloading sequence is very sensitive to the plastic hardening at high strains, as also discussed by GLV (1994), the outcome of this comparison must be considered as satisfactory.

With a method for determining the plastic properties now presented and largely verified experimentally, a corresponding method for the elastic properties deserves some attention. To this end, experimentalists have favoured a formula derived by Sneddon (1945) relating to elastic indentation of a flat circular punch in order to determine the elastic stiffness using the initial slope (dP/dh) of the unloading curve. In view of what has already been discussed in relation to the shape of the elastic and the elastoplastic contact area, using the circular punch results seems to be a somewhat crude approximation. Especially so as King (1987) has derived corresponding formulae for geometrically different flat punches and among them the triangular one which reads

$$E_r = \frac{\sqrt{\pi}}{1.167\sqrt{A_{max}}}\frac{dP}{dh} \tag{19}$$

where A_{max} is the true contact area at maximum indentation load. When comparing the

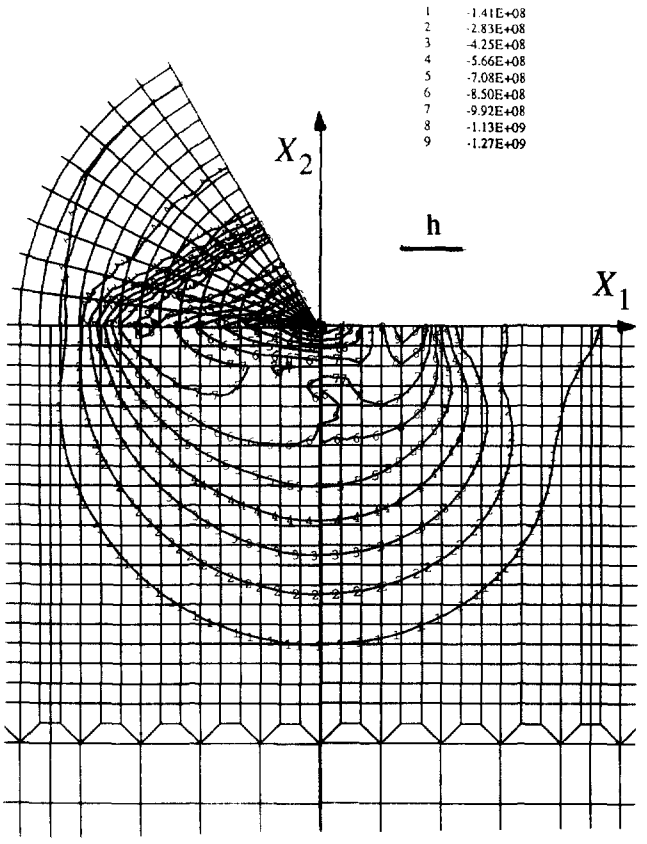

(a)

Fig. 8. Steady state hydrostatic stress for aluminium 7075-T6 (material C) at maximum load. Units are in Pa. The indentation depth h is also shown. (a) Small strain results. (b) Large strain results. The deformation is also shown. (*Continued opposite.*)

elastic stiffness, derived from the explicit values used in the finite element calculations, with the numerically determined ones (using eqn (19)) for the materials A–D the error proved to be −0.7, 3.2, −6.5% (5.0% for the large strain analysis) and 2.0% (3.8% for the large strain analysis) respectively. GLV made the same analysis for the Vickers test [in case of a square contact area the constant 1.167 in eqn (19) changes to 1.142], and found similarly very good agreement for materials with no hardening at high strains but considerably worse results for linear strain hardening materials, mainly owing to the sinking-in of material occuring all around the boundary of contact. Regarding the experimental results, the Instron machine proved to be, as mentioned earlier, insufficiently accurate in the unloading segment due to the larger scatter of results, and in order to check the validity of eqn (19) we used nanoindentation results. The experimentally determined elastic stiffnesses showed almost perfect agreement with the ones obtained from uniaxial compression tests, although a slight size effect was seen also in this case at the lowest loads, and an encouraging conclusion of the present study is that the elastic flat punch unloading formula, eqn (19), can be relied upon to determine the elastic stiffness from a Berkovich test in materials like C and D in Fig. 3. Note, however, that eqn (19) contains the real projected contact area at maximum load, which can be calculated according to $A = 24.56h^2$ as discussed above, so this method differs from the commonly used one where the extrapolated contact depth is used (Doerner and Nix, 1986; Oliver and Pharr, 1992).

At this point some comments about the elastic recovery of the imprint at unloading seems appropriate. As in the Vickers case, the elastic recovery was much more pronounced for hardening materials. Explicit values of the ratio between the recovery at complete unloading and the maximum indentation depth were found to be for material A, 9.6%, for material B, 5.5%, for material C, 12.8% (12.9% for the large strain formulation), and for material D, 7.1%. These values are almost identical to the corresponding Vickers result

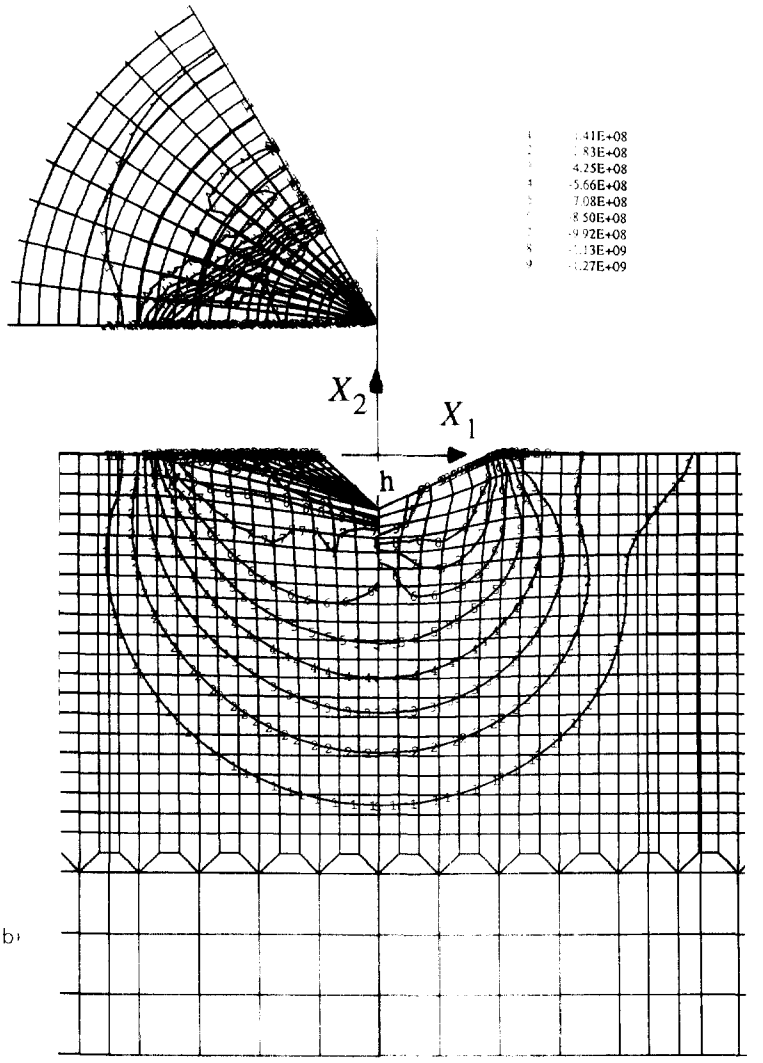

(b)

Fig. [illegible]

and are apparently closely related to the actual stress levels at high plastic strains. This was also confirmed (within 3%) by the experimental load displacement curves, which show that the elastic recovery in depth is about 10% in Al6061, whereas it is about 15% in Al7075 (see Fig. 6d). This observation is in accordance with the larger hardening that Al7075 undergoes in uniaxial deformation compared to Al6061 as shown in Fig. 3. The calculations also showed that the residual imprint left in the material after complete unloading gave essentially the same projected area as the one found numerically at maximum indentation depth. The deformation fields for the large strain calculations, are shown in Fig. 10a and c.

To conclude then the discussion about both axial and local results it remains to comment upon the extent and shape of the plastic zone at Berkovich indentation. For strain hardening materials the elastoplastic boundary, using a small strain formulation, is shown in Figs. 5a and 7a. First of all it is obvious that the zone of plastically deformed material is very close to spherical in accord with the spherical cap approximation by Johnson (1970). Secondly, there is a very good agreement between the extent of the plastic zone at Vickers indentation, GLV (1994), and the one presently derived. The large strain results (Fig. 7b) show a somewhat larger radius of the plastic zone, approximately 9.5% in the X_2-direction, but essentially of the same shape as in Fig. 7a. The size of the plastic zone is, however, strongly dependable on the constitutive properties of the material and a straightforward comparison between material A (no hardening) and material C (linear strain hardening) shows a 35%

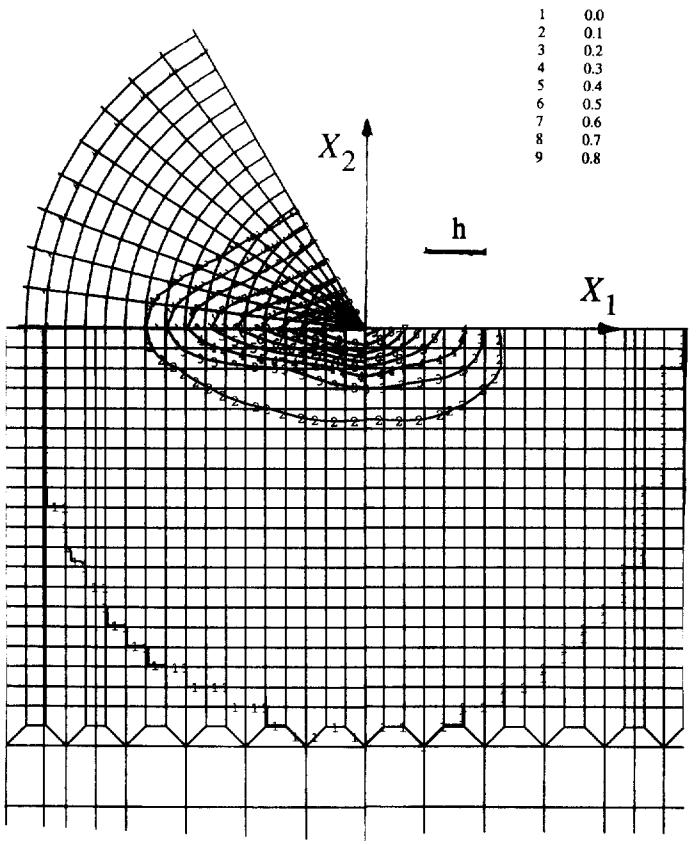

Fig. 9. Steady state accumulated effective plastic strain for aluminium 7075-T6 (material C) at maximum load. The indentation depth h is also shown. (a) Small strain results. (b) Large strain results. The deformation is also shown. (*Continued opposite.*)

increase of the plastic radius when strain hardening is present. Furthermore, this result is also dependable on the yield stress, as a comparison between material B and D shows only 25% increase of the radius in the presence of strain hardening.

We will now turn our attention to the mechanical stress and strain fields involved at Berkovich indentation. For this purpose, we will present results pertinent to Al7075-T6, material C in Fig. 3, and merely comment upon differences, and similarities, in comparison with the other materials. To start with, the field characteristics during the loading process will be discussed. The stress isocontours presented are the von Mises effective stress (Fig. 7) and the hydrostatic pressure (Fig. 8), while the accumulated plastic strain is shown in Fig. 9.

Regarding the isocontours for the von Mises effective stress (σ_e) at loading, as depicted in Fig. 7, they all seem to follow a very regular pattern. The only exception was found in Fig. 7b at the contact area and in a small region close to the edge of contact where in fact unloading occurs. Otherwise, however, almost radial stress distribution was found, which is very interesting from a number of aspects. In particular, it indicates that an analysis using deformation theory of plasticity could give satisfactory results not only for bulk values but also for a more detailed description of the mechanical fields involved. In fact, some preliminary calculations we performed using a Ramberg–Osgood deformation plasticity constitutive equation do indeed point in that direction. Furthermore, some differences in magnitude, but obviously not in shape, can be found between small strain, Fig 7a, and large strain, Fig. 7b, results. Isocontours pertinent to Vickers indentation of material C, GLV (1994), showed essentially the same pattern as the corresponding ones in Fig. 7a. Substantial differences were found, however, when comparing the curves in Fig. 7 with isocontours derived for materials A and B where no plastic hardening is present at strain higher than approximately 6–8%. Indeed, judging from GLV results and the previous discussions about

(b)

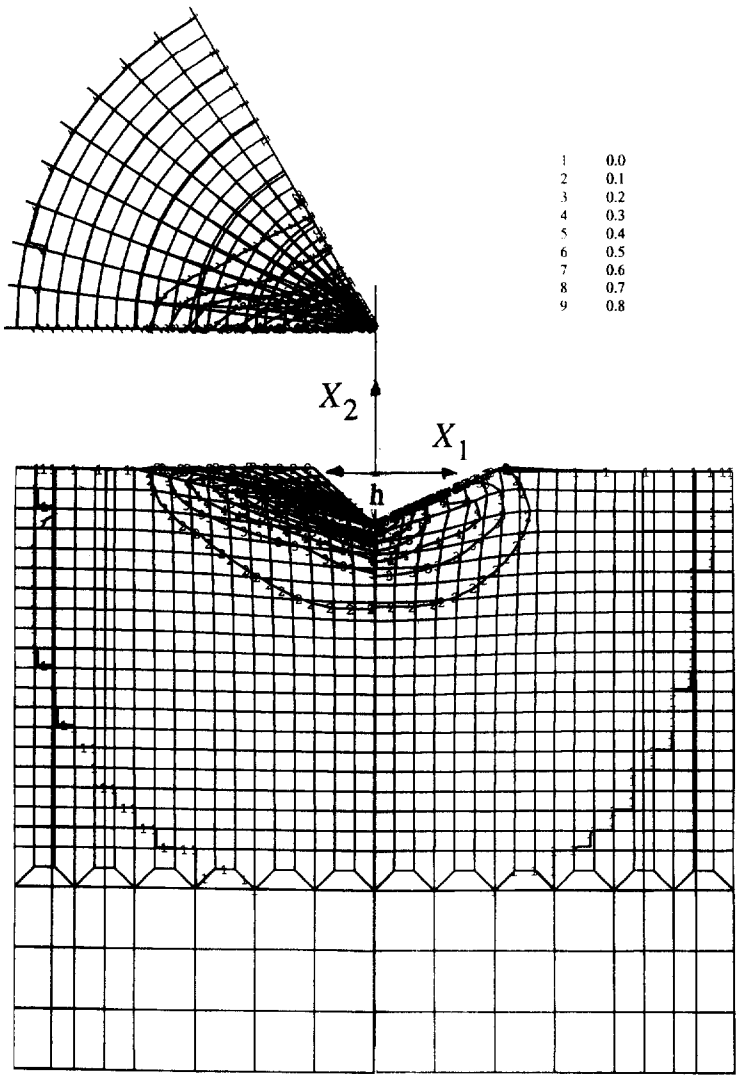

Fig. 9. *Continued*

the size of the plastic zone and the deformation mode at the contact boundary, this could be expected. It was found, for no hardening materials and in accord with the Vickers results, that a local maximum of the von Mises stress occurs below the tip of the indenter. Similar observations were shown for Brinell indentation of plastic, Levy–von Mises, materials by Hill *et al.* (1989) and is also true for Hertz contact between elastic bodies. Furthermore, local unloading occurs at the contact surface, also a feature that was not present at indentation of strain hardening materials.

Now we shift our attention to the isocontours for the hydrostatic pressure, $\sigma_{ii}/3$, as they are depicted in Fig. 8 for both small strain (Fig. 8a) and large strain (Fig. 8b). The small strain results resembles closely the ones derived by GLV for the Vickers test with the maximum compressive stress appearing at the contact surface, unloading at the tip and along the edge of the indenter and with no tensile stresses present. The situation is, however, quite different for the no hardening materials. In this case tensile stresses do develop close to the tip and along the edges of the indenter and thereby creating a possible source for crack formation during loading. Furthermore, for no hardening materials, the maximum compressive stress is found along the X_2-axis below the tip of the indenter and not at the contact area, as was the case for strain hardening materials (Fig. 8). Regarding the large strain isocontours outside the region of contact essentially no difference was found compared to the small strain results. At the tip and along the edge of the indenter, though the

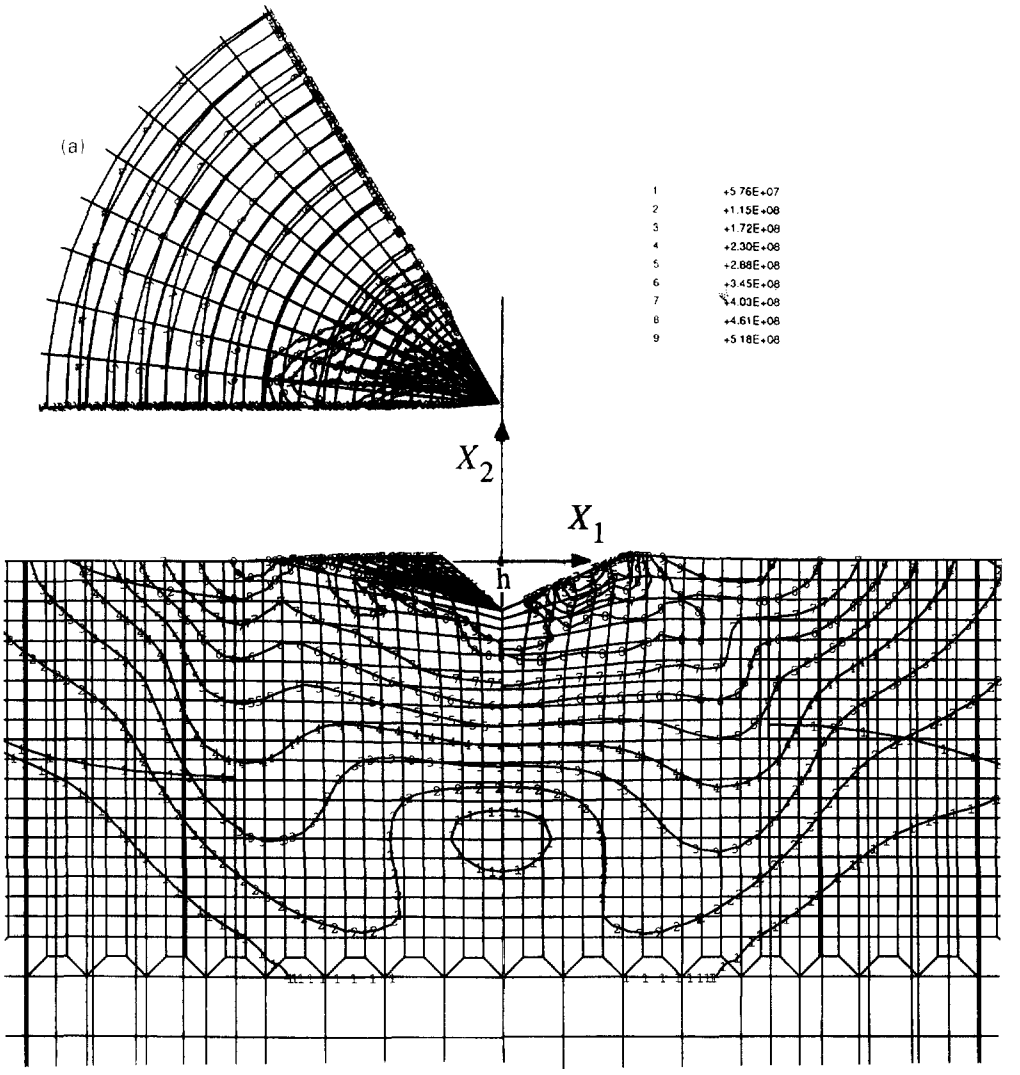

Fig. 10. Stress invariants for aluminium 7075-T6 (material C) after complete unloading. Units are in Pa. The indentation depth h is also shown. (a) Von Mises effective stress (large strain results). The deformation is also shown. (b) Hydrostatic stress (small strain results). (c) Hydrostatic stress (large strain results). The deformation is also shown. (*Continued opposite and overleaf.*)

curves proved to be close to radial and no region of unloading was found. This is an interesting and somewhat surprising result which will be further addressed when discussing possible locations for crack formation and growth.

In Fig. 9 the isocontours of the accumulated plastic strain are shown. Again we can state that these contours for Berkovich indentation are very similar to their corresponding Vickers curves (GLV, 1994) (small and large strain formulation alike). A, perhaps more interesting, result is that at approximately plastic strains of the order of 30% the shape of the isocontours changes. Admittedly, this is not a dramatic effect, in fact it is more pronounced in case of a large strain formulation of the problem, as shown in Fig. 9b, but it does give some further justification for the use of a representative plastic strain 0.3 in eqns (17) and (18). The curves for materials A and B, with no hardening at large plastic strains, resemble closely the ones in Fig. 9.

The final results presented in Fig. 10 are isocontours for the von Mises effective stress (Fig. 10a) (large strain), and the hydrostatic pressure, Fig. 10b (small strain) and Fig. 10c (large strain), after complete unloading of the material. Again the results are pertinent to material C, that is aluminium 7075-T6 with linear plastic hardening at large strains. The von Mises stress curves after complete unloading (Fig. 10a) do not give any new information

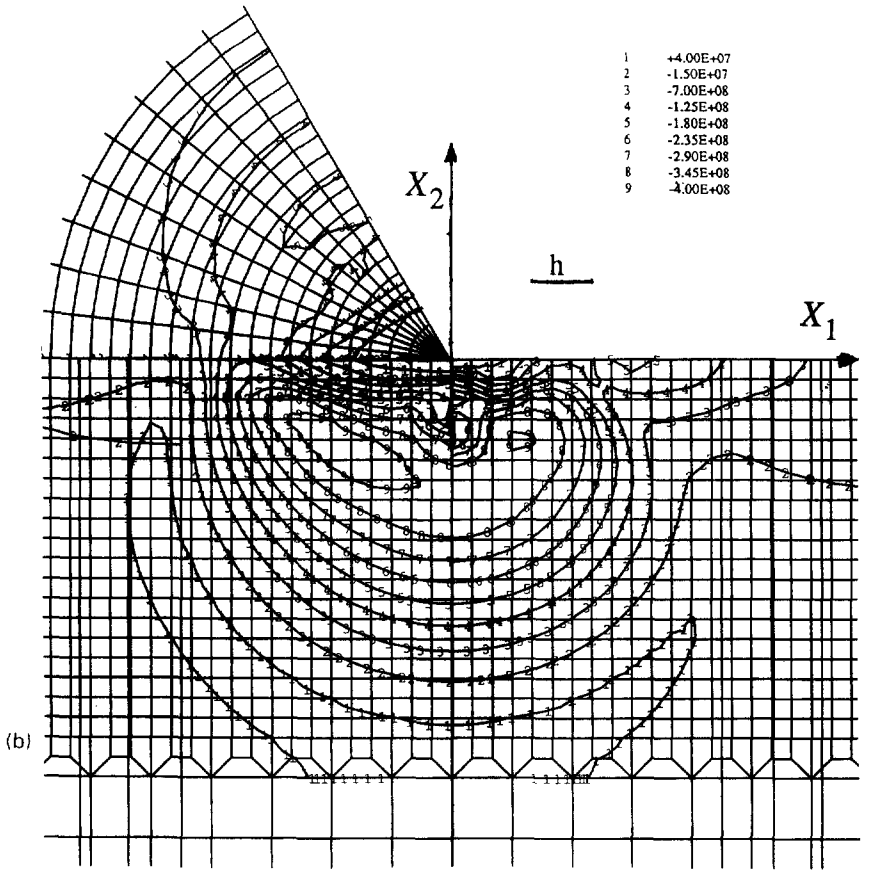

Fig. 10. *Continued.*

of fundamental interest apart from the fact that clearly no reverse plasticity occurs during unloading. Essentially they resemble the Vickers curves derived by GLV with local maxima appearing on the surface outside the contact area and below the tip of the indenter at the X_2-axis. The small strain results were very similar to the ones depicted in Fig. 10a, also close to the area of contact.

The isocontours for the hydrostatic pressure, after complete unloading, are definitely of more direct interest. As can be seen clearly in Fig. 10b regions of tensile stresses develop during unloading even for strain hardening materials. Those regions are not only present at the tip (and especially along the edges) of the indenter but also develop well below the surface, approximately following the boundary between elastic and elastoplastic deformation. The same behaviour was found at Vickers indentation, even though the region of tensile hydrostatic stresses is not only larger in the present analysis but also includes higher tensile pressure levels. It is once again interesting to note that the large strain results in Fig. 10c do not show any region of tensile stresses at the tip of the indenter. Again this has implications for possible crack initiation as will be discussed in some detail below.

It remains then to discuss some aspects of our results related to crack formation during an indentation test. For this purpose we adopted a tough criterium for possible crack formation, demanding that tensile hydrostatic pressure must be present in such a region. This would suggest that for no hardening materials (materials A and B), radial or Palmqvist cracks initiate from the imprint edges during loading while lateral cracks are formed at the elastoplastic boundary below the surface during unloading. For hardening materials (C and D), the hydrostatic stress field does not imply any cracking during loading but instead suggests radial or Palmqvist cracking as well as lateral cracking at the elastoplastic boundary below the surface when unloading is performed. It should be emphasized though that radial/Palmqvist cracking is, for the material characteristics presently analysed, a feature of the small strain formulation of the problem and no evidence for such crack systems were

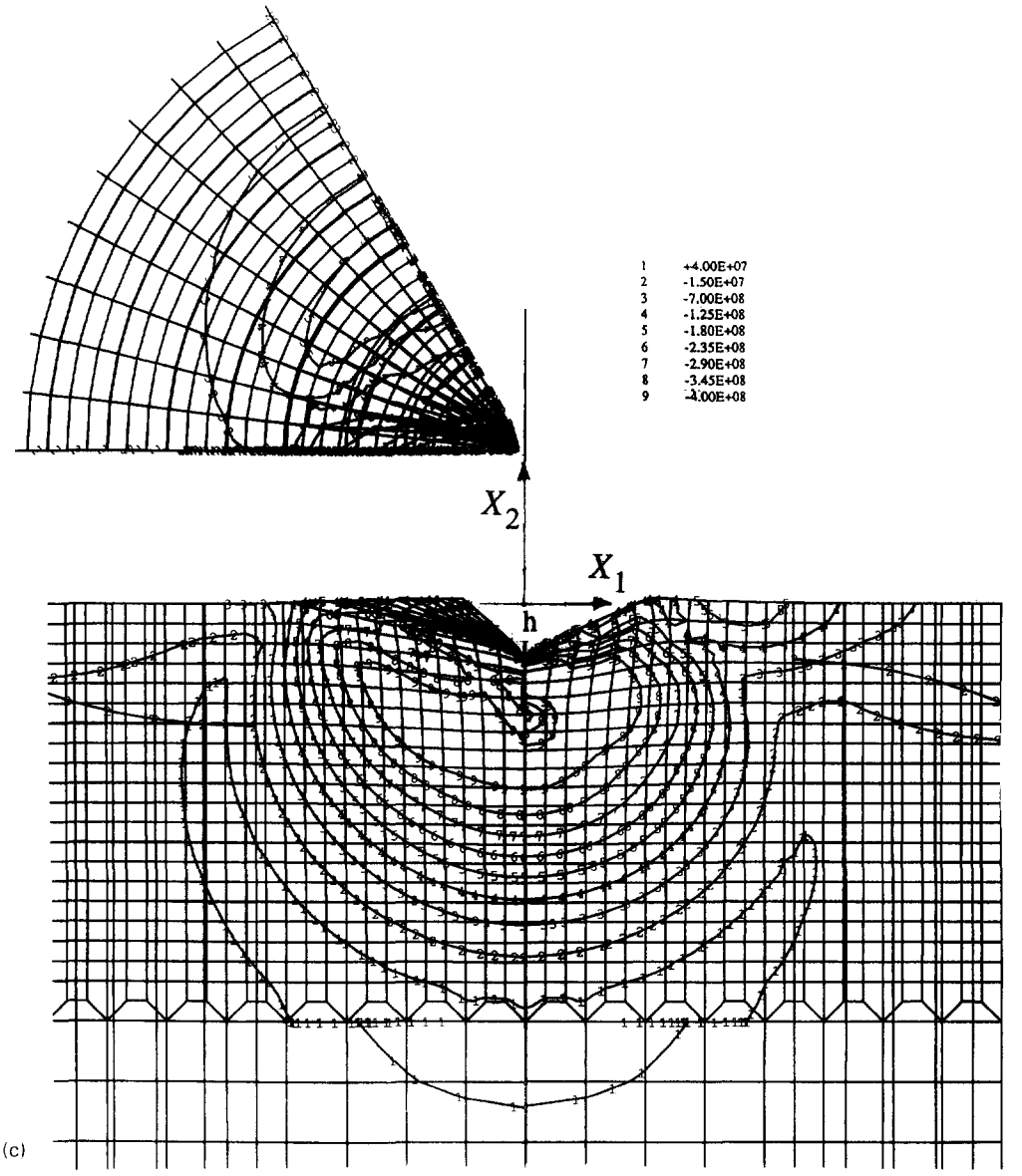

Fig. 10. *Continued.*

found when analysing the large strain numerical, or the experimental, results, neither at loading nor at unloading. However, experimental observations of radial crack formation have been reported by among others Cook and Pharr (1990), but in that case for ceramic materials. Other possible crack geometries during an indentation test are half-penny cracking and cone cracking. Presently, for the Berkovich indenter, owing to geometrical reasons, half-penny cracking can not be predicted, and we found little or no evidence when examining either the hydrostatic pressure or the maximum principal stress for cone cracking around the indenter. One possible explanation for this is the fact that we assume frictionless contact in our analysis, whereas friction might be, as shown by Andersson (1994) for Brinell indentation, a driving force for cone crack initiation. It should be remembered though, that the materials most pertinent to the discussion above are brittle ones, for example ceramics, where von Mises plasticity alone may not be an appropriate constitutive description. The present results can, however, at least give some qualitative information of possible locations for crack formations and the sequence of cracking for such materials with loading.

6. CONCLUSIONS

Berkovich indentation of elastic and elastoplastic materials was analysed numerically and experimentally. Universal formulae for hardness and total indentation load were derived from the numerical results showing excellent agreement with experimental findings. Formulae for determining the elastic stiffness at initial unloading were checked numerically and found to be reliable regardless of the plastic hardening present, at least for the range of moderate hardening investigated presently. Mechanical stress and strain fields were presented showing among other things the size and shape, found approximately spherical, of the plastic zone and possible locations for crack growth. However, the plastic strain distribution did not form the commonly assumed concentric spheres. Also the contact area between material and indenter was computed and proved to be a hyperbola (using six-fold symmetry) at elastic indentation and almost triangular at elastoplastic indentation.

The Berkovich and Vickers indentation tests proved to be closely related. The main difference concerned the mode of deformation at the boundary of contact where the effect of plastic strain hardening was much less pronounced at Berkovich indentation. This feature also has implications when determining the elastic stiffness at initial unloading as it indicates that the Berkovich test is more favourable for this purpose, due to the substantially smaller amount of sinking-in of material at the contact boundary.

Most features of Berkovich indentation were found to be well captured within a small strain formulation of the governing equations. For example, the small strain universal formulae for hardness and total indentation load proved to be valid also for results derived using a large strain formulation of the problem, if simply scaled by a factor of 1.1. However, for a detailed description of the mechanical fields close to the contact area a large strain analysis is certainly needed, a feature of importance in particular when crack formation and growth are of interest.

As for the experimental results the nanoindenter proved to be especially suitable for obtaining accurate load–displacement curves, and in particular for determining elastic material constants during the unloading part of the indentation cycle. The nanoindentation results clearly exhibited size effects for the analysed materials, indicating that higher applied loads were needed in order to obtain bulk macroscopic plastic material properties. An important conclusion from the study is that the effects from piling-up and sinking-in cancel each other in Berkovich indentations large enough to cover several grains. This means that the yield stress and the characteristic stress at 30% plastic strain can be derived from the hardness numbers obtained either from total depth under load or from optical measurements of the real residual area. The constitutive behaviour, thus, can be determined from load–displacement curves obtained by stiff and accurate indentation systems, operating at high enough loads.

Acknowledgement—The authors would like to thank the National Supercomputer Centre in Sweden for the opportunity to use the CRAY X-MP 416 supercomputer at the University of Linköping.

REFERENCES

ABAQUS users manual. Version 5.2 (1992). Hibbitt, Karlsson & Sorensen, Inc., Providence, RI.

Andersson, M. (1994). Licenciate Thesis. Department of Solid Mechanics, Royal Institute of Technology, Stockholm, Sweden.

Barber, J. R. and Billings, D. A. (1990). An approximate solution for the contact area and elastic compliance of a smooth punch of arbitrary shape. *Int. J. Mech. Sci.* **32**, 991–997.

Bilodeau, G. G. (1992). Regular pyramid punch problem. *J. Appl. Mech.* **59**, 519–523.

Cook, R. F. and Pharr, G. M. (1990). Direct observation and analysis of indentation cracking in glasses and ceramics. *J. Am. Ceram. Soc.* **73**, 787–817.

Doerner, M. F. and Nix, W. D. (1986). A method for interpreting the data from depth-sensing indentation instruments. *J. Mater. Res.* **1**, 601–609.

Dukino, R. D. and Swain, M. V. (1992). Comparative measurement of indentation fracture toughness with Berkovich and Vickers indenter. *J. Am. Ceram. Soc.* **75**, 3299–3304.

Giannakopoulos, A. E., Larsson, P.-L. and Vestergaard, R. (1994). Analysis of Vickers indentation. *Int. J. Solids Structures* **31**, 2679–2708.

Gibson, L. J. and Ashby, M. F. (1988). *Cellular Solids—Structure and Properties*. Pergamon Press, Oxford.

Hallbäck, N. (1993). Licenciate Thesis. Department of Solid Mechanics, Royal Institute of Technology, Stockholm, Sweden.

Hill, R., Storakers, B. and Zdunek, A. B. (1989). A theoretical study of the Brinell hardness test. *Proc. R. Soc. Lond.* **A423,** 301–330.

Johnson, K. L. (1970). The correlation of indentation experiments. *J. Mech. Phys. Solids* **18,** 115–126.

King, R. B. (1987). Elastic analysis of some punch problems for a layered medium. *Int. J. Solids Structures* **23,** 1657–1664.

Kral, E. R., Komvopoulos K. and Bogy, D. B. (1993). Elastic-plastic finite element analysis of repeated indentation of a half-space by a rigid sphere. *J. Appl. Mech.* **75,** 829–841.

Laursen, T. A. and Simo, J. C. (1992). A study of the mechanics of microindentation using finite elements. *J. Mater. Res.* **7,** 618–626.

Loubet, J. L., Georges, J. M., Marchesini, O. and Meille, G. (1984). Vickers indentation curves of magnesium oxide (MgO). *J. Tribology* **106,** 43–48.

Maiden, C. J. and Green, S. J. (1966). Compressive strain-rate tests on six selected materials at strain rates from 10^{-3} to 10^{4} in in sec. *J. Appl. Mech.* **88,** 496–504.

Mayo, M. J. and Nix, W. D. (1988). A micro-indentation study of superplasticity in Pb, Sn, and Sn-38 wt% Pb. *Acta Metall.* **36,** 2183–2192.

Mayo, M. J., Siegel, R. W., Narayanasamy, A. and Nix, W. D. (1990). Mechanical properties of nanophase TiO_2 as determined by nanoindentation. *J. Mater. Res.* **5,** 1073–1082.

Oliver, W. C. and Pharr, G. M. (1992). An improved technique for determining hardness and elastic modulus using load and displacement sensing indentation experiments. *J. Mater. Res.* **7,** 1564–1583.

Pethica, J. B., Hutchings, R. and Oliver, W. C. (1983). Hardness measurements at penetration depths as small as 20 nm. *Philos. Mag.* **A48,** 593–606.

Rowcliffe, D. J. (1991). Quasi-static indentation of ceramics. In *Erosion of Ceramic Materials* (Edited by J. E. Ritter). Trans. Technical Publications.

Sneddon, I. N. (1945). Boussinesq's problem for a flat-ended cylinder. *Proc. Cambridge Philosophical Soc.* **42,** 29–39.

Storakers, B. and Larsson, P.-L. (1994). On Brinell and Boussinesq indentation of creeping solids. *J. Mech. Phys. Solids* **42,** 307–332.

Söderlund, E., Reineck, I. and Rowcliffe, D. J. (1994). Ultralow load indentation hardness and modulus of κ- and α-Al_2O_3 CVD coatings. *J. Mater. Res.* **9,** 1683–1692.

Tabor, D. (1951). *Hardness of Metals.* Clarendon Press, Oxford.

Williams, M. L. (1952). Stress singularities resulting from various boundary conditions in angular corners of plates in extension. *J. Appl. Mech.* **74,** 526–528.